

**SAND2015-XXXXR**

**LDRD PROJECT NUMBER:** 166153

**LDRD PROJECT TITLE:** Upscaling ab-initio chemistry models to non-equilibrium flow simulations

**PROJECT TEAM MEMBERS:** Marat Kulakhmetov, Alina Alexeenko, and Daniel Rader

## **ABSTRACT:**

Thermochemical nonequilibrium is generated by hypersonic cruise vehicles, high speed combustion and detonations. Nonequilibrium interactions affect reaction rates and energy transfer that are critical for many engineering applications. Ab-initio potential energy surfaces can be used in quasi-classical trajectory (QCT) calculations to calculate state-specific dissociation rates and cross sections, as well as state-to-state energy exchange rates and cross sections. These rates and cross sections are needed for simulating such nonequilibrium flows. However, there are two main challenges in extending QCT calculations to modeling all chemical processes found in typical engineering flowfields. First, ab-initio surfaces for many collision partners are not available and when available their fidelity is not quantified. Second, state-to-state cross section datasets are typically on the order of  $1000^4$ , and are too large to be efficiently implemented in engineering simulations. This work focuses on  $O_2+O$  interactions because of prevalence of oxygen in many engineering application; however, all of the models developed here may be applied to other diatom-atom interactions and can be extended to other diatom-diatom combinations. It is shown in this work that at temperatures between 2,500 and 20,000K, state-specific cross sections are not highly sensitive to potentials and a Morse additive pairwise (MAP) potential is proposed for modeling collisions for which ab-initio potentials are not available. Next, this work suggests an approach to model state-to-state cross sections based on maximum entropy considerations. The calculated cross sections are fit to a new model with just 8 parameters, which can be easily scaled up to flow simulations.

## **INTRODUCTION:**

Many advanced engineering technologies involve nonequilibrium reacting flows. Such flows are generated by re-entry vehicles, scramjets, micro-devices, plasma environments and detonations. (Reising, et al. 2014) (Maruta 2011) During Earth re-entry gas temperature in the shock region exceeds 10,000 K, which leads to air dissociation. (Park 1989) The flow in the shock is highly nonequilibrium and chemical kinetics there cannot be characterized by single-temperature Arrhenius rates. Flight conditions and trajectories that generate thermochemical nonequilibrium can be found in Fig. 1. The nonequilibrium, shown in orange, is typically generated at flight velocities above 2 km/s and it will persist at velocities above 10 km/s. Above 10 km/s, flowfield ionization and radiation can become significant even though they are not considered in this work. As can be seen, ascent, reentry, and orbital transfer vehicles are likely to experience nonequilibrium.

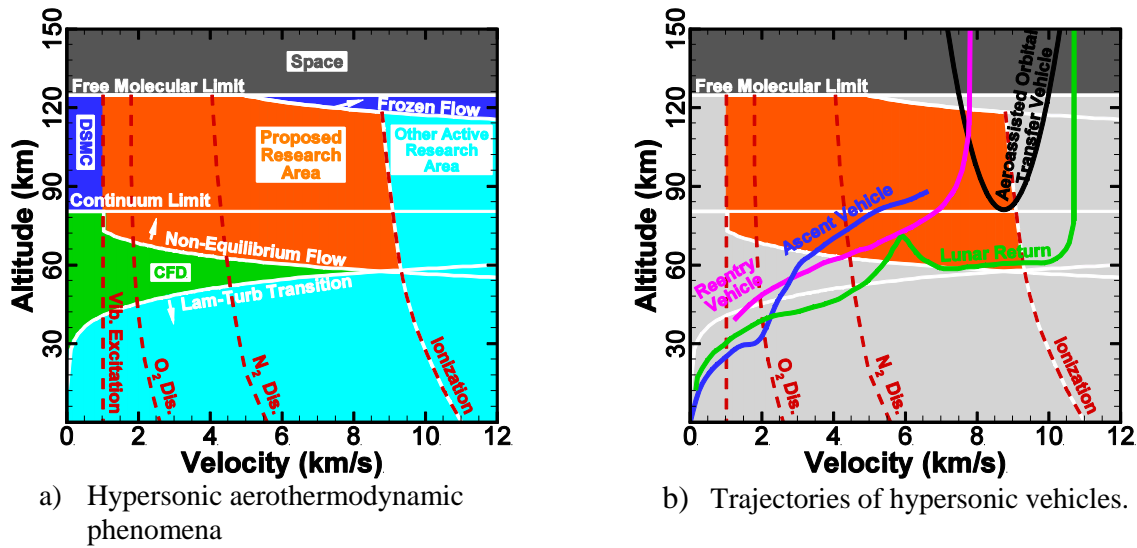


Figure 1: A survey of hypersonic vehicles and aerothermodynamic phenomena they experience. The current work focuses on flows with thermo-chemical nonequilibrium. The figure is generated for a vehicle with a 5 m reference length and 0.5 m reference features (M. Kulakhmetov 2014) (Harris, Millman and Greendyke 1992) (Bertin 1994) (Laurendeau 2005) (I. Levine 2000) (Park 1989) (Kulakhmetov, Alina, et al. 2012)

There is currently a lack of high-fidelity nonequilibrium air chemistry models that can account for internal energy specific chemical reaction and relaxation processes. Due to the difficulty of measuring high energy collisions experimentally, modern computational fluid dynamics (CFD) and direct simulation Monte Carlo (DSMC) codes predominately depend on phenomenological collision models. (G. Bird 1994) (G. Bird 2011) (Haas and Boyd 1993) (Wadworth and Wysong 1997) These models are often calibrated to reproduce equilibrium measurements, such as transport coefficients or reaction rates, but they are not guaranteed to be accurate in nonequilibrium regimes. Furthermore, hypersonic flight may generate shock temperatures in excess of 30,000 K, while experimental measurements seldom exceed 10,000K. This is highlighted in a survey of oxygen dissociation measurements that is found in Table 1. When high temperature data is not available, measurements taken at lower temperatures are extrapolated to the higher temperatures with unknown uncertainty.

Table 1: A Survey of High Temperature Oxygen Reaction Rate Experiments			
Technique	Temperature Range (K)	Uncertainty	Reference
Interferometer	3,000 - 5,000	50 %	(Mathews 1959)
Interferometer	2,800 - 5,000	20 %	(Byron 1959)
1550 A absorption	4,000 - 9,000	N/A	(Schexnayder and Evans 1961)
X-Ray absorption	3,000 - 6,000	20 %	(Rink, Knight and Duff 1961)
200-2700 nm absorption	4,000 - 10,800	N/A	(Ibraguimova, et al. 2013)

Detailed State-specific energy exchange and dissociation cross sections can be calculated from the well-established quasi-classical trajectory (QCT) method. (Karplus, Porter and Sharma 1965) (Truhlar, Muckerman and Bernstein 1979) This method has been used by the chemistry community for decades to study a wide range of reacting systems and the results have been verified against quantum calculations. (Gilibert, et al. 1992) (Braunstein, et al. 2003) Within the last two decades there has been an increased interest in adapting QCT calculations to chemically reacting flows in reentry applications. This method has been used to study  $N_2+N$ , (Jaffe, Schwenke and Chaban 2009) (Kim and Boyd 2014) (Esposito and Capitelli 2006),  $N_2+N_2$ , (Panesi, Jaffe and Schwenke 2013) (Parsons, et al. 2014)  $O_2+O$ , (Esposito and Capitelli 2002) (Esposito, Armenise, et al. 2008), and other chemical systems, (Gimelshein, Levin and Gimelshein 2003), at high enthalpy conditions. There are two main challenges in upscaling these ab-initio QCT calculations to full flowfield simulations. First, the trajectory calculations require a potential energy surfaces (PES) for all interacting particles. Ab-initio potential energy surfaces are often constructed by performing detailed electronic structure calculations for discrete atomic positions and fitting the results to analytic functions. However, there are over half a dozen species even in simple reacting air flows and more than two dozen possible collision partner combinations. (Park 1989) High enthalpy flows may be further complicated by ablating species, increasing both collision pair combinations and the required number of PES. The second challenge stems from the fact that air molecules have thousands of discrete internal states. Therefore, QCT calculations can produce  $> (1000)^4$  state-to-state cross sections. A dataset that large cannot be used efficiently in a flow simulation and reduced model are need for such calculations.

Although many of the required potential energy surfaces are not available, these could be constructed based on spectroscopic measurements using just two-body interaction terms. (Koura 1998) (Norman, Valentini and Schwartzentruber 2013) Such simplified potential, composed of Morse terms, is referred to as Morse additive pairwise (MAP) potential in this report. Although the simplified potentials are missing complex 3-body interaction features, the potential energy of these features are often smaller than total energy of hypervelocity collisions and they may not significantly affect collision dynamics. This work investigates the sensitivity of high temperature ( $T>2,500$  K)  $O_2+O$  dissociation and energy exchange processes to potential energy surfaces. Results from ab-initio and simplified potential energy surfaces are compared to experimentally measured equilibrium dissociation rates.

There are a few approaches discussed in literature to handle state-to-state cross sections within CFD and DSMC. The most direct approaches were taken by Kim and Boyd and Norman et. al. The former authors tabulated a complete set of  $N_2+N$  cross sections and sampled them within direct simulation Monte Carlo (DSMC) collision steps. (Kim and Boyd 2014) In the latter case, the authors performed entire classical trajectory calculations for each DSMC collision step in order to outcome of all collisions. (Norman, Valentini and Schwartzentruber 2013) Although these two methods offer the highest accuracy, the former case is difficult to scale up because the dimensionality of state-to-state cross sections grows rapidly as more collision pairs are considered and the latter case significantly increases costs of flow calculations. Another common approach is to combine state-specific cross sections into large bins and then recompute bin-to-bin rates. This approach is pursued by Parson et al. and Panesi et al. (Parsons, et al. 2014) (Panesi, Jaffe and Schwenke 2013). Although this approach is promising, large bins decrease the resolution of state-

specific processes. In this work we investigate fitting state-to-state cross sections to a new model based on the maximum entropy considerations. (Levin and Bernstein 1987) More discussion on this approach is presented in the discussion section.

The analysis in this work focuses on the  $O_2+O$  collision. This chemical system has been studied extensively by the chemistry community in order to understand the formation of ozone. A survey of  $O_3$  chemical dynamics studies is presented by Schinke et al. (Schinke, et al. 2006) However, most of that work considered gas temperatures below 1,000 K, while many engineering problems involve gas temperature that ranges between 1,000 - 20,000 K. Esposito et. al. (Esposito and Capitelli 2002) have used the  $O_3$  double many-body expansion (DMBE) PES by Varandas and Pais (Varandas and Pais 1988) to calculate  $O_2+O$  vibrational relaxation and dissociation rates at temperatures up to 10,000 K. Their works showed good agreement with experimentally-measured equilibrium dissociation rates. Therefore, the Varandas and Pais PES is used as a benchmark surface here. This surface is compared to a Morse additive pairwise (MAP) potential that is constructed based on  $O_2$  spectroscopic constants.

## DETAILED DESCRIPTION OF EXPERIMENT/METHOD:

At the fundamental level, atomic interactions are described the by Schrodinger wave equation (SWE), (I. Levine 2000)

$$H(R,r)\Psi(R,r) = E\Psi(R,r), \quad (1)$$

where  $\psi(R,r)$  is the total wave function that depends on both nuclear,  $R$ , and electron,  $r$ , coordinates,  $E$  is the total system energy and  $H$  is the system Hamiltonian. The Hamiltonian,

$$H = T_{nuc}(R) + T_{el}(r) + V_{nn}(R) + V_{ne}(R,r) + V_{ee}(r), \quad (2)$$

includes nuclear kinetic energy,  $T_{nuc}(R)$ , electronic kinetic energy,  $T_{el}(r)$ , nuclear repulsion energy,  $V_{nn}(R)$ , electronic repulsion energy,  $V_{ee}(r)$ , and nuclear-electron attractive energy  $V_{ne}(R,r)$ , operators. Analytical solutions to the SWE exist only for simple one electron atoms. (Wolfgang 2006) For all other atoms and molecules the SWE has to be solved numerically. The dimensionality and computational cost of this system grows quickly as the number of atoms and electrons, increases. Due to the high computational expense, the SWE cannot be used to model even the simplest flowfield.

By realizing that the nuclei are heavier and slower than electrons, the Eq. 1 can be separated into electronic,

$$(T_{el}(r) + V_{ne}(R,r) + V_{ee}(r))\psi(R,r) = W(R)\psi(R,r) \quad (3)$$

and nuclear equations,

$$(T_{nuc}(R) + V_{nn}(R) + W(R))\chi(R) = E\chi(R) \quad (4)$$

This separation is known as the Born-Oppenheimer approximation. (Hirst 1985) Eq. 3 is used to solve for the electronic potential energy,  $W(R)$  at fixed nuclear coordinates,  $R$ . This electronic potential could then be used to solve the nuclear wave function. In practice, Eq. 3 is often solved at a set of discrete nuclear coordinates and then those are fit to a response surface. The summation of  $V_{nn}(R)$  and  $W(R)$  terms produces the potential energy surface (PES) that describes the motion of atoms in an electron cloud. Such PES for  $N_2+N_2$ ,  $N + NO$ ,  $O+O_2$ ,  $N_2+N_2$  have been calculated by numerous authors. (Lagana, Garcia and Ciccarelli 1987) (Walch and Jaffe 1987) (Jaffe, Schwenke and Chaban 2010) The  $O_2+O$  surfaces used in the present work are described in more detail further on.

Once the PES is generated, particle collision dynamics can be solved using quantum and quasi-classical approaches. The former approach initializes wave functions in the quantum states of interest and then propagates these using the unsteady SWE (Sanz-Sarna and Portillo 1996) (Kormann, Holmgren and Karlsson 2008). In quasi-classical approaches, initial quantum ro-vibrational levels are related to classical atomic positions and momentum. Once initialized, atomic trajectories are integrated using classical equations of motion and final atomic positions and momenta are used to determine collision outcomes.

### Quasi Classical Trajectories

In this work,  $O_2+O$  scattering, state-to-state and dissociation cross sections are calculated using the quasi-classical trajectory (QCT) method. This method is described in detail by Karplus et al. (Karplus, Porter and Sharma 1965) and Truhlar et al. (Truhlar, Muckerman and Bernstein 1979) therefore we only briefly discuss our implementation of the method here.

The trajectories of an atom-diatom collisions are propagated classically using the Hamiltonian equations of motion,

$$\frac{dQ_i}{dt} = \frac{\partial H}{\partial P_i}, \quad (5)$$

and

$$\frac{dP_i}{dt} = -\frac{\partial V}{\partial Q_i}, \quad (6)$$

where  $Q_i$  are generalized coordinates,  $P_i$  are generalized momentum coordinates that correspond to  $Q_i$  and  $V$  is the potential energy. The first three generalized coordinates,  $[Q_1, Q_2, Q_3] = R_{BC}$ , describe the intramolecular bond between atoms B and C, while the next three describe the position between the free atom, A from the center of mass of the molecule BC,  $[Q_4, Q_5, Q_6] = R_{A-BC}$ . These coordinates are visualized in Fig. 2. The total energy of a diatom (B-C) colliding with an atom (A) in generalized coordinates can be calculated as



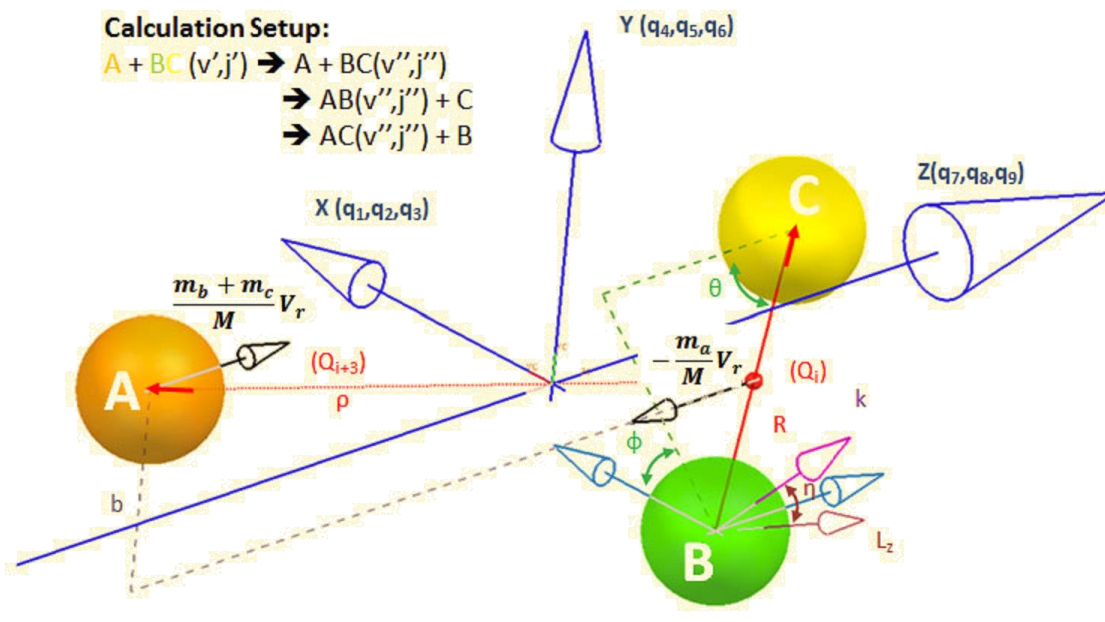


Figure 2: QCT collision coordinates.

$$H = \frac{1}{2\mu_{bc}} \sum_{i=1}^3 P_i^2 + \frac{1}{2\mu_{a,bc}} \sum_{i=1}^3 P_{i+3}^2 + V(Q), \quad (7)$$

using reduced masses:  $\mu_{bc} = (m_b m_c)/(m_b + m_c)$  and  $\mu_{a,bc} = (m_a)(m_b + m_c)/(m_a + m_b + m_c)$ . The classical coordinates are related to initial quantum ro-vibrational energies,  $E_{rv}(v, J)$  by solving for the maximum intramolecular bond stretch,  $R_m = |R_{BC}|$ ,

$$\frac{J(J+1)\hbar^2}{2\mu_{bc}R_m^2} + V(R_m) = E_{rv}(v, J). \quad (8)$$

In Eq. 8,  $v$  and  $J$  are initial vibrational and rotational levels. Initial trajectory coordinates are fully defined by these energy levels, 2 molecular orientation angles, a phase angle, rotational momentum angle, impact parameter and relative velocity. These additional parameters are also shown in Fig. 2 although more information can be found in (M. Kulakhmetov 2014)

In our implementation, trajectories defined by Eq. 5 and 6 are propagated from initial coordinates classically using the 5th-6th order Runge-Kutta method with a variable time step. Once the colliding particles move outside the collision shell,  $\rho$ , the integration stops and we determine if a reaction happened. For stable product molecules we first quantize angular momentum,  $J'$ , and then solve for a ro-vibrational level with energy  $E_{rv}(v', J')$  equivalent to the classical energy of the

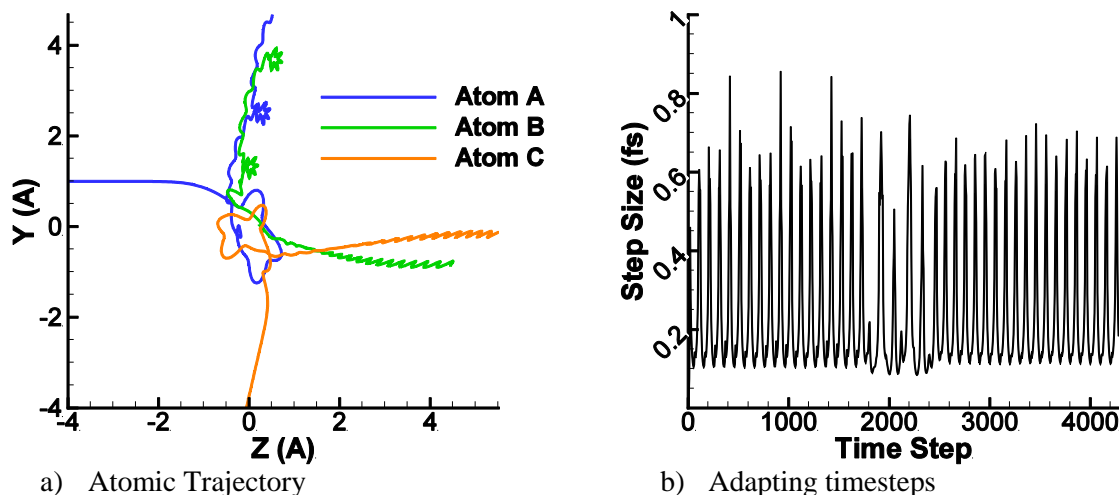


Figure 3:  $O_2 + O$  collision with  $b = 1.5 \text{ Å}$ ,  $V_r = 3 \text{ km/s}$ ,  $\theta = \Phi = \Psi = \eta = \pi/2$ ,  $J = 11$ ,  $V = 10$

molecule. If our ro-vibrational levels are not integers then we round them to the closest integer and place the excess energy into the post-collision translational energy,  $E'_t$ . A sample collision trajectory and adapting timesteps are shown in Fig. 3.

The reaction probability,  $P_r$ , can be calculated from QCT outcomes,  $O_r$ , by averaging the outcomes over all initial conditions:

$$P_r(V_r, v, J) = \frac{1}{b_{max}^2 (2\pi)^3} \int_{\zeta=0}^{2\pi} \int_{\eta=0}^{2\pi} \int_{\phi=0}^{2\pi} \int_{\theta=0}^{\pi} \int_{b=0}^{b_{max}} O_r(b, \theta, \phi, \eta, \zeta, V_r, v, J) b db \sin(\theta) d\theta d\phi d\eta d\zeta. \quad (9)$$

The subscript,  $r$ , in probabilities,  $P_r$ , and collision outcomes,  $O_r$ , refers to a generic process of interest. For inelastic state-to-state processes, the subscript  $r$  is replaced with  $(v', J')$ , denoting the final  $v'$  and  $J'$  ro-vibrational level. The collision outcome,  $O_r$ , equals to 1 when under collision conditions  $(b, \theta, \phi, \eta, \zeta, V_r, v, J)$  the process  $r$  occurs and 0 otherwise. The QCT outcomes,  $O_r$  in Eq. 9 are averaged over equal cross section areas,  $b db$ ; the initial molecular orientation is averaged over equal solid angles,  $\sin(\theta) d\theta d\phi$ , vibrational phase angle,  $\zeta$ , and rotational momentum orientation,  $\eta$ , are uniformly distributed.

A cross section is a reference area, centered at the second particle, through which a first particle needs to pass to cause a reaction. This reaction may be a molecular dissociation, atomic exchange or molecular excitation/de-excitation. A cross section can be calculated as:

$$\sigma_r(V_r, v, J) = \pi b_{max}^2 P_r(V_r, v, J). \quad (10)$$

Here, the maximum impact parameter,  $b_{\max}$ , needs to be chosen so that at  $b=b_{\max}$  no reactions occur. Small  $b_{\max}$  values can be used if we are only interested in dissociation cross sections while larger values are needed to resolve scattering probabilities.

Specific rates in binary collisions can be calculated by averaging the product of reaction cross sections and relative velocities,  $V_r$  in a collision:

$$k_r^{v,J}(T) = \overline{\sigma_r(V_r, v, J)V_r} = \int_0^\infty \sigma_r(V_r, v, J)V_r f(V_r) dV_r. \quad (11)$$

The superscripts (v,J) refer to the initial ro-vibrational level of the colliding molecule. Equilibrium rates can be calculated from state specific rates by averaging the latter over the equilibrium ro-vibration distribution functions.

$$k_r(T) = \frac{\sum_{v=0}^{V_{\max}} \sum_{J=0}^{J_{\max}(v)} k_f^{v,J} (2J+1) \exp\left(\frac{-E_{rv}(v, J)}{kT}\right)}{\sum_{v=0}^{V_{\max}} \sum_{J=0}^{J_{\max}(v)} (2J+1) \exp\left(\frac{-E_{rv}(v, J)}{kT}\right)}. \quad (12)$$

In Eq. 12  $V_{\max}$  is the maximum possible vibrational level,  $J_{\max}(v)$  is the maximum possible rotational level for a given vibrational level,  $(2J+1)$  is the rotational degeneracy, and  $E_{rv}(v, J)$  is the energy of the ro-vibrational level (v, J). The maximum ro-vibrational levels can be calculated directly from each PES.

In aerothermodynamics, nonequilibrium rates are often reported using two or three temperature models. To compare to these, non-equilibrium rates in this work are calculated as:

$$k_r(T_t, T_v, T_r) = \frac{\sum_{v=0}^{V_{\max}} \exp\left(\frac{-E_v(v)}{kT_v}\right) \sum_{J=0}^{J_{\max}(v)} k_f^{v,J}(T_t) (2J+1) \exp\left(\frac{-E_r(v, J)}{kT_r}\right)}{\sum_{v=0}^{V_{\max}} \exp\left(\frac{-E_v(v)}{kT_v}\right) \sum_{J=0}^{J_{\max}(v)} (2J+1) \exp\left(\frac{-E_r(v, J)}{kT_r}\right)}, \quad (13)$$

where:  $T_t$ ,  $T_v$  and  $T_r$  are translational, vibrational and rotational temperatures,  $E_v(v) = E_{rv}(v, J=1)$ , and

$$E_r(v, J) = E_{rv}(v, J) - E_{rv}(v, J=1). \quad (14)$$

At equilibrium conditions,  $T=T_t=T_r=T_v$ , Eq 12 and 13 match exactly. In two temperature models  $T=T_t=T_r$  and  $T_v \neq T$ . In practice, the multi-dimensional integrals in 9 and 11 are solved using the Monte Carlo method:



$$\sigma_r(V_r, v, J) = \pi b_{max}^2 \sum_N \frac{O_r(b_i, \theta_i, \phi_i, \eta_i, \zeta_i, V_r, v, J)}{N}$$

$$k_r^{v,J}(T) = \sqrt{\frac{8\pi kT}{m_r}} \sum_N \frac{O_r(b_i, \theta_i, \phi_i, \eta_i, \zeta_i, V_r, v, J)}{N}, \quad (15)$$

where input variables are sampled as:

$$\begin{aligned} b &= \sqrt{R_f} b_{max} \\ \theta &= \arccos(1 - 2R_f) \\ \phi &= 2\pi R_f \\ \eta &= 2\pi R_f \\ \zeta &= 2\pi R_f \\ V_r &= \sqrt{\frac{2kT}{m_r} \ln(R_f * R_f)}, \end{aligned} \quad (16)$$

More description on Monte Carlo sampling of trajectories can be found in (M. Kulakhmetov 2014) Integration time step tolerance and the maximum impact parameter are determined from a cross section convergence study. The calculated mono-quantum de-excitation cross sections are verified against those reported by Esposito et al. (Esposito, Armenise, et al. 2008) for the same potential. Our calculations matched within 5% for most of the collision energy range. The largest difference between the reported and our calculations is 35%, occurring at the collision energy of 0.01 eV, where the statistical noise is higher. A complete flow diagram of our QCT code is found in Fig. 4. The outer loop in this algorithm is skipped when equilibrium rates are not necessary and the two outer loops are skipped when only cross sections are needed.

### Potential Energy Surfaces:

The results of a QCT calculation depend on the potential used. Two O<sub>3</sub> potential energy surfaces are considered in this work: a Morse additive pairwise (MAP) potential and a double many-body expansion (DMBE) potential obtained by Varandas and Pais. (Varandas and Pais 1988) The MAP potential is a summation of two-body Morse terms,

$$V_{MAP} = \sum_{i=1}^2 \sum_{j=i+1}^3 D_{i,j} \left( \left[ 1 - \exp\{-\beta_{i,j}(R_{i,j} - R_{e,i,j})\} \right]^2 - 1 \right), \quad (17)$$

where i and j are summation indices over all atoms, R<sub>i,j</sub> is the distance between atoms i and j, R<sub>e,i,j</sub> is the equilibrium bond length, D<sub>ij</sub> is the potential well depth, and β<sub>i,j</sub> determines the potential well width. The Morse parameters for the ground electronic level are summarized in table 2 based on values suggested by Konowalov and Hirschfelder for oxygen. (Konowalov and Hirschfelder 1961) These parameters are derived from spectroscopic data by Vanderslice et al. (Vanderslice, Mason and Maisch 1960) The MAP potential is easy to construct and is computationally inexpensive to evaluate during trajectory calculations. The vibrational energy for the MAP potential is evaluated as:

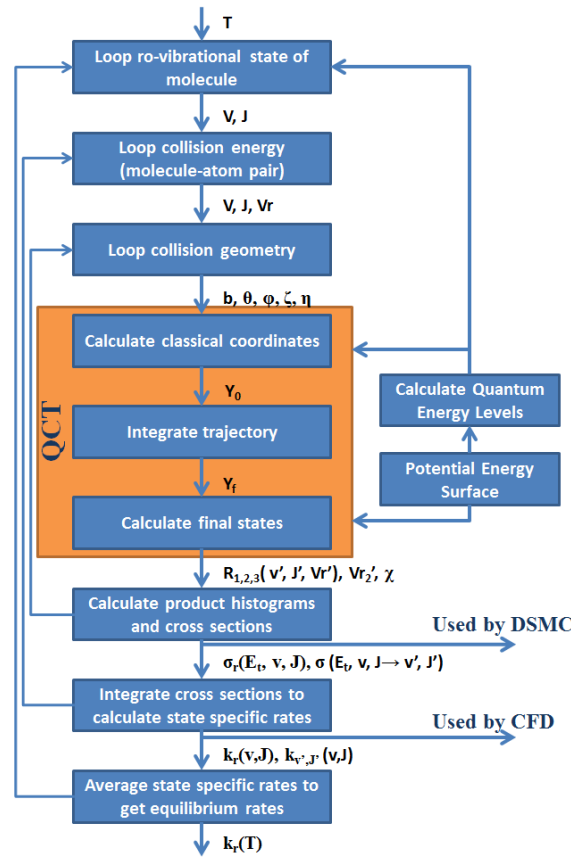


Figure 4: Flow diagram for calculating cross sections and reaction rates.

$$E_v(v) = w_e(v + 1/2) + w_e x_e(v + 1/2)^2 \quad (18)$$

with constants:  $w_e$  and  $w_e x_e$ , tabulated by Laurendeau. (Laurendeau 2005) based on spectroscopic data. These constants can be found in table 2 as well. The ro-vibrational energy for both potentials is calculated as:

$$E_{rv}(v, J) = E_v(v) + B_v J(J+1) - D_e J^2(J+1)^2, \quad (19)$$

where,

$$B_v = B_e - a_e(v + 1/2). \quad (20)$$

with constants:  $w_e$  and  $w_e x_e$ , tabulated by Laurendeau (Laurendeau 2005) based on spectroscopic data. These constants can be found in table 2 as well. The ro-vibrational energy for both potentials is calculated as:

$$E_{rv}(v, J) = E_v(v) + B_v J(J+1) - D_e J^2(J+1)^2, \quad (21)$$

where,

$$B_v = B_e - a_e(v+1/2). \quad (22)$$

The additional constants:  $a_e$ ,  $B_e$ , and  $D_e$ , can also be found in table 2.

The Varandas-Pais potential is a DMBE fit of experimental and ab-initio data for ground state ozone. The potential is composed of 2-body and 3-body extended Hartree-Fock (EHF) and correlation terms. Most of the potential terms and parameters could be found in (Varandas and Pais 1988) whose authors graciously provided us an updated version of the potential. This potential surface has 36 fitting coefficients and in general it is about 20 times more expensive to evaluate, compared to the MAP potential. Esposito et al. (Esposito, Armenise, et al. 2008) calculated vibrational levels,  $E_v(v)$ , for this potential using the WKB method and tabulated them. These vibrational levels are used in Eq. 20 while rotational levels are modeled using the same parameters ( $B_v$ ,  $D_e$ ) as used for the MAP potential. These rotational constants can be found in table. 2.

The two potentials for collinear collisions are shown in Fig. 5. Since the MAP is just a summation of 2-body interaction terms, it is missing saddle points and has a deeper  $O_3$  equilibrium well. This potential predicts that a stable ozone molecule will have an equilateral-triangular structure and will require 10.4 eV to dissociate  $O_3$  to  $O_2+O$ . However, it is known that ozone is a bent triatomic with a bond angle of  $117^\circ$  and a 1.1 eV dissociation energy. (Schinke, et al. 2006) It is also important to point out that the close-range repulsive part of the Varandas and Pais potential is convex while it is concave on the MAP potential. The next section of this paper investigates the effect of differences in potentials on  $O_2+O$  collisions in the 2,000 - 20,000 K temperature range.

Ab-initio potential energy surfaces are typically calculated with atoms in specified electronic states. Likewise, the MAP potential is built based on  $O_2$  spectroscopic constants for the  $O_2$  ground electronic level. However, at 20,000 K, the  $O_2+O$  collision energies may exceed a few eVs, making excited electronic levels accessible. Disregarding electronic excitation will lead to errors in dissociation and energy exchange rates. For example, without the electronic correction factor,

**Table 2: Reduced Dimensionality Morse Potential Parameters for Molecular Oxygen ( $X^3\Sigma$ ). The data is by Konowalow and Hirschfelder (Konowalow and Hirschfelder 1961) and Laurendeau. (Laurendeau 2005)**

<b>D</b>	5.211 eV
<b><math>R_e</math></b>	1.207 Å
<b><math>\beta</math></b>	2.78 Å <sup>-1</sup>
<b><math>w_e</math></b>	0.1955 eV
<b><math>w_e x_e</math></b>	0.0011 eV
<b><math>B_e</math></b>	1.4456 cm <sup>-1</sup>
<b><math>a_e</math></b>	0.0159 cm <sup>-1</sup>
<b><math>D_e</math></b>	4.84E-6 cm <sup>-1</sup>

equilibrium dissociation rates calculated by the Varandas and Pais potential are up to a factor of 4 lower than experimental rates by Shatalov in the 5,000 K to 10,000 K temperature range.

There are a few techniques discussed in literature that consider electronic excitations in classical trajectory calculations. The most rigorous technique is the trajectory surface hopping (TSH) that has been advanced by Tully. (Sholl and Tully 1998) This technique; however, requires potential surfaces for all excited electronic levels and coupling potentials, which seldom exist. Other authors perform separate trajectory calculations on each electronic surface independently and then average the results. (Brunsvold, et al. 2008) However, determining the averaging weights for results from each surface is not trivial. This work follows the method proposed by Truhlar, (Truhlar 1972) and used previously by Varandas (Varandas and Pais 1988) and Esposito (Esposito and Capitelli 2002) for  $O_2+O$  collision studies. In the absence of electronic surfaces that correlate to all reactants, a single ground electronic PES is used for trajectory calculations. The calculated state-to-state rates and cross sections are then multiplied by a ratio of degeneracy of the ground PES to degeneracies of the reactants. The  $O_3(X^1A)$  DMBE Varandas and Pais surface used in this work has a degeneracy of 1. The reactants are the ground  $O_2$  in the  $^3\Sigma$  state that has a degeneracy of 3 and the ground  $O$  in the  $^3P$  state that has the degeneracy of 9. Therefore the state-to-state cross sections calculated based on the Varandas and Pais potential need to be scaled by  $1/(3*9)=1/27$ . Although this correction is simple, Tashiro and Schinke (Tashiro and Schinke 2003) tested it for the complex forming  $O+O_2$  collisions and concluded that the single surface match multisurface calculations within 30% for collision energies up to 0.1 eV. The authors are not aware of similar tests for higher energy collisions. Since the final cross sections need to be scaled by a constant and the goal of the present work is to compare cross sections calculated via different potentials, the state-to-state vibrational cross sections presented in this work are not scaled. The proper scaling constant could

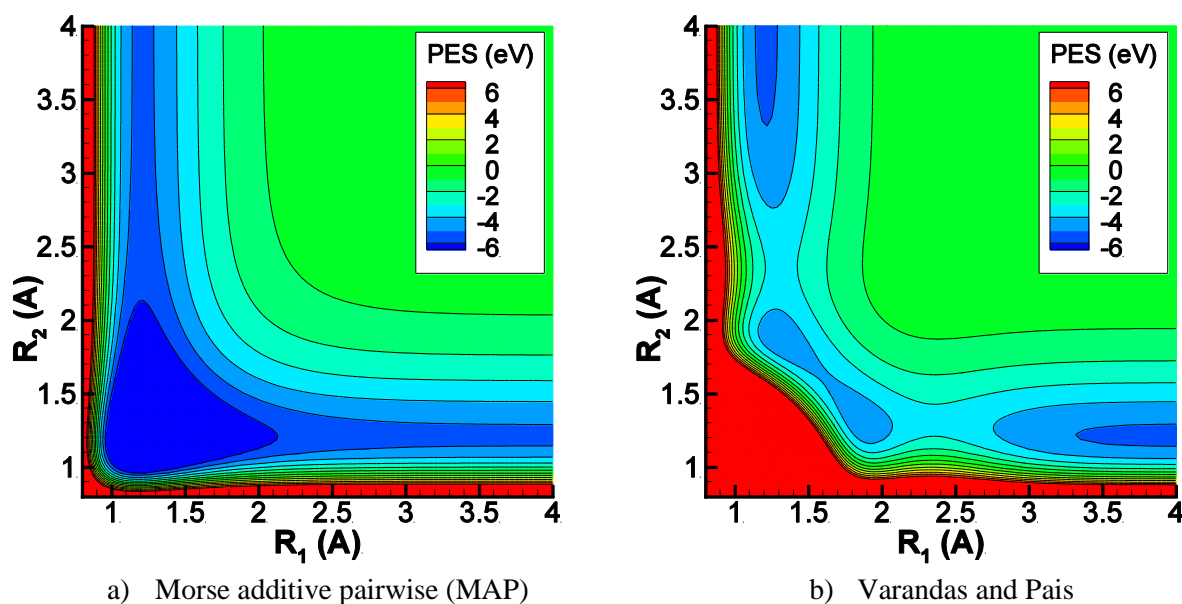


Figure 5: Potential energies for a collinear collision.  $R_1$  is the distance between atoms 1 and 2, while  $R_2$  is the distance between atoms 2 and 3

be calibrated by comparing to experimentally measured vibrational relaxation rates, when available.

Nikitin (Nikitin 1974), Esposito and Capitelli (Esposito, Armenise, et al. 2008) suggest that ro-vibrational modes of different electronic levels remain in an approximate equilibrium during dissociation. The ratio of dissociations from the ground electronic level to dissociations from other electronic levels simply depends on the degeneracy ratio of the electronic levels. Therefore, dissociation rates and cross sections are calculated in this work using the ground electronic surfaces but they are then scaled by a factor of  $G$ .

$$G = \sum_{i=1}^{E_{rv}(v,j) < E_i} g_i / g_1. \quad (23)$$

The summation of electronic degeneracies,  $g_i$  in Eq. 21, is over all stable electronic levels with energies,  $E_i$ , below the ro-vibrational energy,  $E_{rv}(v,J)$ . These degeneracies can be found in table 3 for the ground and seven excited electronic levels.

## RESULTS AND DISCUSSION:

### Sensitivity of dissociation rates and cross sections

Dissociation cross sections calculated via the two potentials are compared in Fig. 6. In general, the two potentials predict similar cross sections while the translational energy is below 6 eV even though the two potentials are significantly different. For instance, the  $v=10$  and  $v=20$  dissociation cross sections for a 5 eV translational energy calculated via the two potentials differ by less than 10%. Collision dynamics in this energy range are not significantly affected by 3-body interaction part of the potential. For collision energies above 6 eV, the Morse potential under predicts reaction cross sections. These differences can be explained by comparing the repulsive parts of the potentials in Fig. 5. The Varandas potential is more likely to scatter high energy reactants into the

**Table 3: Electronic degeneracies of oxygen. Parameters obtained by Esposito and Capitelli (Esposito and Capitelli 2002)**

State	Energy (eV)	Degeneracy
$X^3\Sigma_g^-$	-5.10	3
$a^1\Delta_g$	-3.84	2
$b^1\Sigma_g^+$	-3.15	1
$c^1\Sigma_u^-$	-1.02	1
$C^3\Delta_u$	-0.81	6
$A^3\Sigma_u^+$	-0.72	3
$B^3\Sigma_u^-$	1.14	3
$2^3\Pi_g$	1.98	6



fully dissociated state (upper right corner) while the MAP potential is more likely to scatter the reactants back toward the entry corridor (lower right corner). The high energy cross sections can be improved by modifying the repulsive part of the potential; however, it is difficult to predict these corrections a priori without some ab-initio calculations. (Kulakhmetov and Alexeenko 2015) Although the Varandas and MAP dissociation cross sections deviate for translational energies above 6 eV, high-energy deviations do not significantly affect macroscopic reaction rates at temperatures up to 20,000 K. Reaction rates are obtained by integrating dissociation cross sections with translational energy distribution functions, Eq. 11 and 12. These distribution functions, which can be seen in Fig. 6 for  $T = 10,000$  and  $20,000$  K, drop off rapidly for high translational energies. Less than 1% of collisions at 10,000 K and 17% of collisions at 20,000 K have translational energies above 6 eV and therefore the deviation in dissociation cross sections does not significantly affect dissociation rates. To illustrate this further, the equilibrium  $O_2 + O \rightarrow 3O$  dissociation rates are calculated by averaging state-specific dissociation rates over roughly 2,800 ro-vibrational levels. In turn, each state-specific rate is obtained from 500 trajectory calculations. Therefore, each equilibrium rate is based on roughly 1.4 million trajectories and they include quasi-bound initial states. As shown in Fig. 7 the equilibrium rates

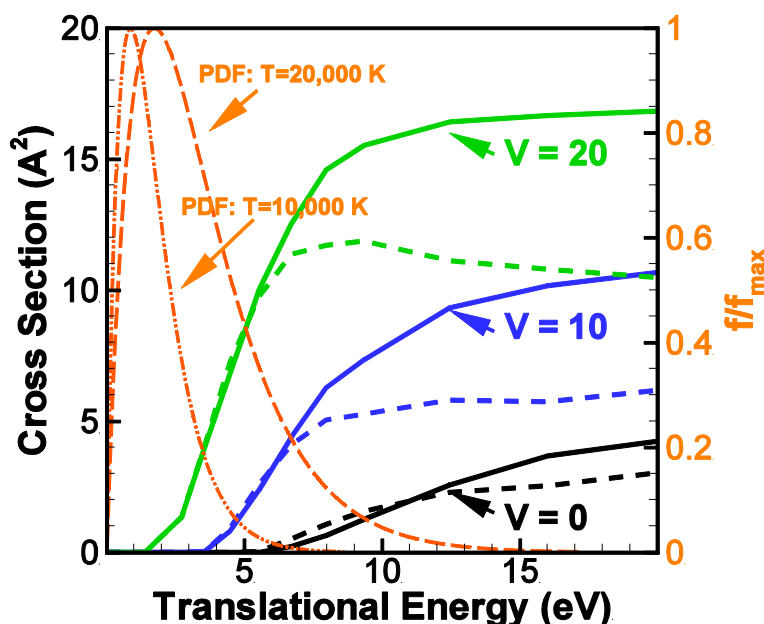


Figure 6:  $O_2 + O \rightarrow 3O$  dissociation cross sections calculated via the Varandas and Pais potential (solid lines) and the MAP potential (dashed lines). The rotational level is maintained at 11, which is the mean level at  $T_r = 300$  K. Translational energy distribution functions, shown in orange for  $T = 10,000$  K and  $T = 20,000$  K, demonstrate that high energy deviations in cross sections do not significantly affect dissociation rates

are calculated every 2,500 K, from 2,500 K to 20,000 K using the DMBE Varandas and the MAP potentials. Rates calculated via the two potentials match within 12% at temperatures in the studied temperature range. These differences in rates cannot be distinguished from the sampling statistical uncertainty, which is estimated to be approximately 30%. If the dissociation rates are calculated by analytically fitting and integrating cross sections in Fig. 6 then at 20,000 K dissociation rates can be shown to deviate by up to 14 %.

Since reaction rates for many high enthalpy flows are uncertain by an order of magnitude (Park 1989) the rates compared here are in good agreement. The QCT-calculated rates are bound by the experimental measurements of Shatalov (Esposito and Capitelli 2002) and Ibraguimova. (Ibraguimova, et al. 2013) The uncertainty in rates caused by using the MAP potential is much smaller than experimental measurement disagreement (300 % at 10,000 K).

As can be seen in Fig. 7, the mean rates calculated by the Varandas and Pais and MAP potentials are 40% lower than those reported by Shatalov, (Esposito, Armenise, et al. 2008) at temperatures up to 10,000 K. The standard deviation of sampled state specific rates is approximately 30% of the mean values. Because of the lack of experimental measurements above 10,000 K, dissociation rates above this temperature are compared to those suggested by Park. (Park 1989) Park produced a compilation of rates based on a survey of available experimental data and a model to extrapolate these rates to higher temperatures. Between 10,000 K and 20,000 K, the QCT rates are 30% to 70% higher than Park rates.

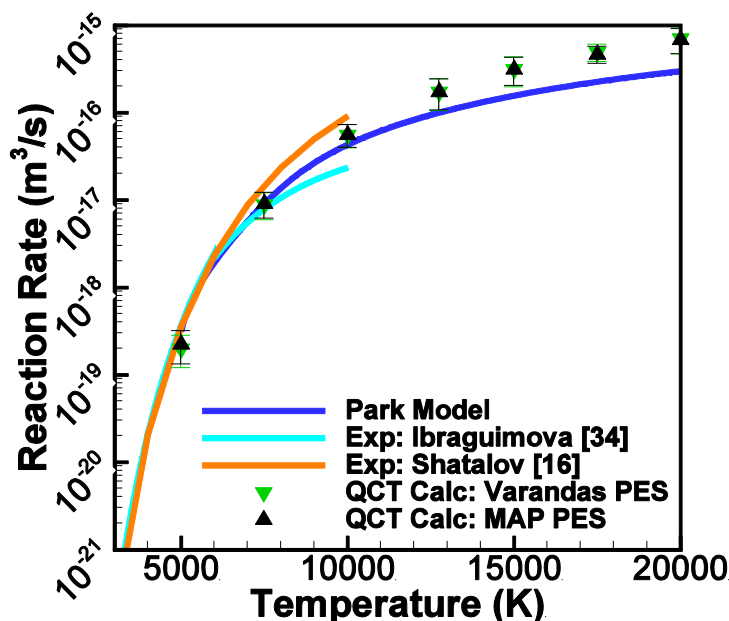


Figure 7:  $O_2+O \rightarrow 3O$  equilibrium dissociation rates calculated via the Varandas and Pais and MAP potentials. Experimental measurements are found in (Esposito and Capitelli 2002) (Ibraguimova, et al. 2013)

The sensitivity of nonequilibrium dissociation rates to PES is studied next. Two-temperature ( $T=T_t=T_r$ ,  $T_v \neq T$ ) rates are calculated by assuming that translational and rotational levels follow Maxwell and Boltzmann distributions at temperature  $T$  while the vibrational levels follow a Boltzmann distribution at  $T_v$ . As can be seen in Fig. 8, the nonequilibrium rates calculated via the MAP and Varandas and Pais potentials at  $T=5000$  K are within 10% at vibrationally hot conditions ( $T_v>T$ ) and within 70% at vibrationally cold conditions ( $T_v<T$ ). This comparison improves significantly as the translational temperature increases and at  $T=20,000$  K, the two are within 20% in the entire vibrational temperature range.

The QCT-calculated nonequilibrium rates are also compared to those predicted using Park's model. This model uses the Arrhenius equation for modeling non-equilibrium rates but with a modified effective temperature. This effective temperature in the Park's model is calculated via the geometric average,

$$T_a = \sqrt{TT_v}, \quad (24)$$

as suggested by Park and via the kinetic theory definition of average temperature,

$$T_a = \frac{3T_{tr} + \zeta_{rot}T_{rot} + \zeta_{vib}T_{vib}}{3 + \zeta_{rot} + \zeta_{vib}}, \quad (25)$$

as suggested by Gallis et al. (Gallis, R. and Torczynski 2010) Although the QCT and Park equilibrium rates match within 37%, the standard Park nonequilibrium rates differ from the QCT rates by 60% at vibrationally hot conditions and by over two orders of magnitude at vibrationally cold conditions. Vibrationally cold conditions are expected in shock layers generated by re-entry vehicles and the lower reaction rates would lead to hotter shock cap temperatures. With geometric averaging, as the vibrational temperature approaches zero, so does the effective temperature. Therefore, the rate of the original Park model drops quickly for low vibrational temperatures. Physically; however, at low vibrational temperatures only the ground vibrational levels of  $O_2$  are populated and dropping the vibrational temperature further should not affect the nonequilibrium rates. These trends are reproduced by the QCT calculations in Fig. 8. The low vibrational temperature performance of the Park's model is improved by using the kinetic theory temperature averaging, in which  $\zeta_{rot}=2$ ,  $\zeta_{vib} = 1$ . However, this averaging method leads to lower vibrationally hot and higher vibrationally cold temperatures, suggesting that this scheme does not lead to enough vibrational favoring. The vibrational favoring can be improved somewhat by defining an unphysically high vibrational degrees of freedom ( $\zeta_{vib} = 4$ ), although this model cannot reproduce all of the trends observed from the QCT calculations.

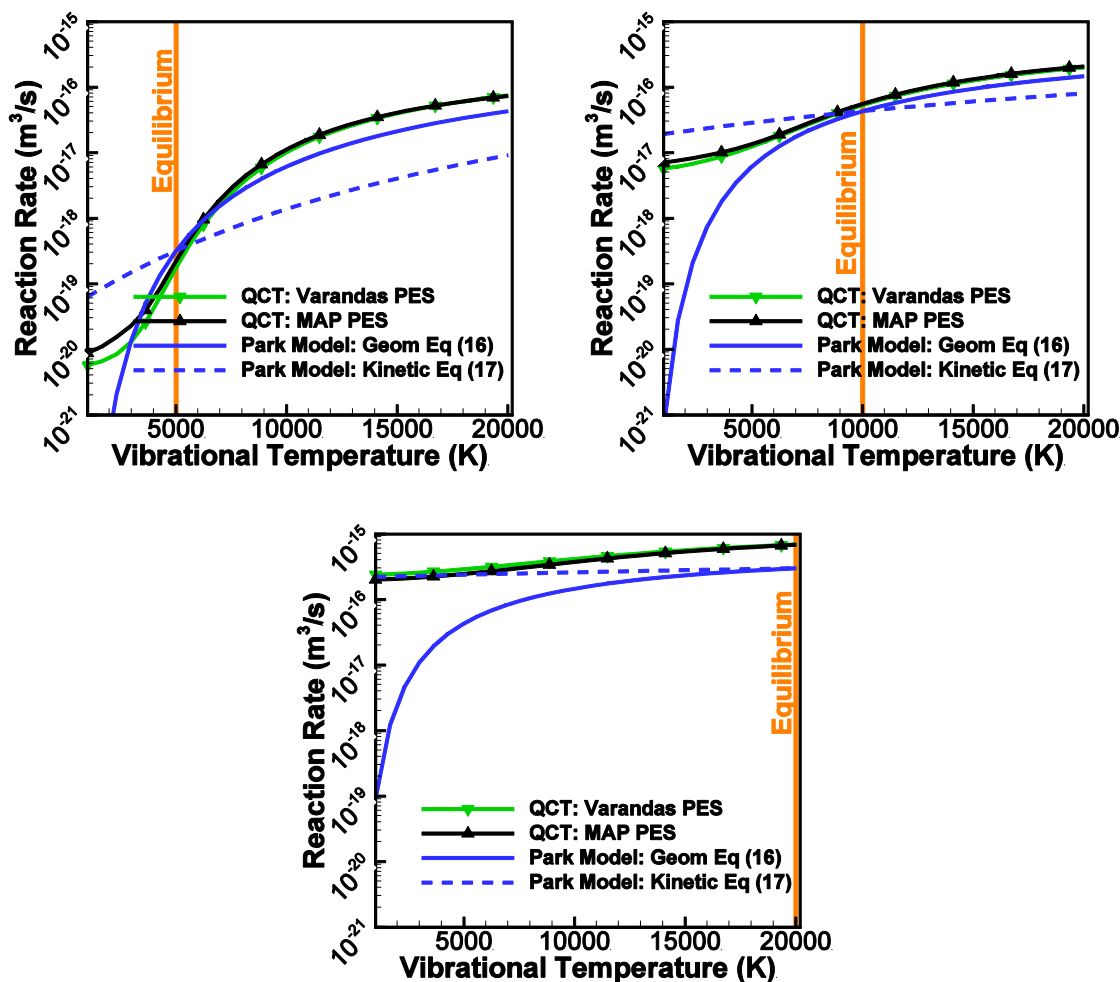


Figure 8: Two-temperature ( $T=T_t=T_r$ ,  $T_v \neq T$ )  $\text{O}_2 + \text{O} \rightarrow 3\text{O}$  nonequilibrium dissociation rates for  $T=5,000$ ,  $10,000$  and  $20,000$  K. Thermal equilibrium is denoted by an orange line. Lower temperature rates are vibrationally cold while higher temperature rates are vibrationally hot.

As already mentioned, rates predicted by nonequilibrium phenomenological models deviate by over two orders of magnitude in the vibrationally cold conditions ( $T_v < T$ ) yet rates calculated using the two potentials deviate by less 70%. Therefore, using a MAP instead of ab-initio potential provides rates that are more accurate than current phenomenological models. When ab-initio potentials are calculated, most effort should be devoted to the close-range repulsive parts, since they contribute the most to state-specific dissociation cross sections.

## Sensitivity of state-to-state internal energy exchange

The state-to-state vibrational cross sections are compared next. The cross sections for initial  $v=0$  and  $v=10$  can be found in Fig. 9. These cross sections are calculated for  $J=11$  rotational level and are averaged over all final rotational levels. In general, the shape of state-to-state cross sections calculated via the two potential are similar although the Varandas and Pais potential predicts more elastic collisions while the MAP potential predicts higher de-excitation cross sections. For instance,  $\sigma(v=10, J=11, V_r=1\text{km/s} \rightarrow v'=0) = 0.06\text{\AA}^2$  for the MAP potential and  $0.02\text{\AA}^2$  for the Varandas and Pais potential. Therefore, the MAP-calculated cross sections will lead to a faster flow relaxation rates. The differences in cross sections decrease as the collision velocity is increased. As can be seen in Fig. 9b, the difference in relaxation cross sections decreased to 10% when the relative velocity increases to 7 km/s. The vibrational state-to-state cross sections also match better when initial vibrational energy increases.

The comparison between state-to-state rotational cross sections is presented in Fig. 10a for  $J=11$  initial rotational level and in Fig. 10b for  $J=51$  initial level. In all cases presented, the initial vibrational level is maintained at 0, although cross sections for higher vibrational levels are also calculated. Just as before, the two potentials predict similar excitation cross sections although the MAP potential predicts higher de-excitation cross sections. For  $V_r=3\text{ km/s}$  relative velocities ( $E_t = 0.50\text{ eV}$ ), de-excitation cross sections differ by up to a factor of 5; however, when the  $V_r$  increases to 5 km/s ( $E_t=1.38\text{ eV}$ ), the maximum difference drops to a factor of 2. The comparison improves

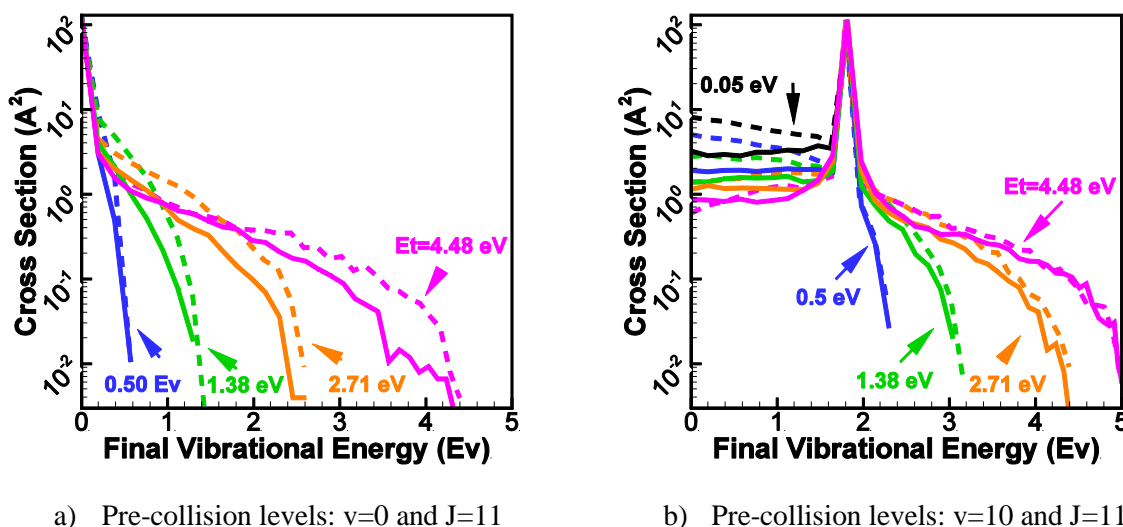


Figure 9: Comparison of state-to-state vibrational cross sections calculated via the Varandas and Pais (solid lines) and MAP (dashed lines) potentials for translational energies:  $E_t = 0.05\text{ eV}$ ,  $0.5\text{ eV}$ ,  $1.38\text{ eV}$ ,  $2.71\text{ eV}$ ,  $4.48\text{ eV}$ . Note, electronic corrections are not applied in these plots.



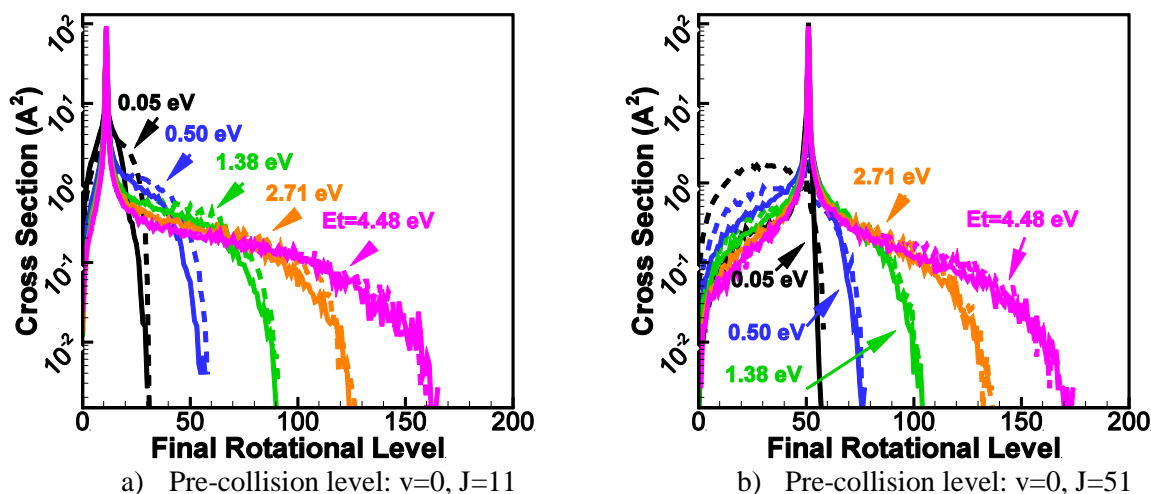


Figure 10: Comparison of state-to-state rotational cross sections calculated via the Varandas and Pais (solid lines) and MAP (dashed lines) potentials for translational energies:  $E_t = 0.05$  eV,  $0.5$  eV,  $1.38$  eV,  $2.71$  eV,  $4.48$  eV. Note, electronic corrections are not applied in these plots.

significantly when the relative velocity or initial vibrational level are increased further. The differences in rotational cross sections above  $V_r = 7$  km/s ( $E_t = 2.71$  eV) or  $v = 30$  (not shown in plots) are indistinguishable from statistical noise.

The MAP potential over predicts vibrational and rotational de-excitation for collision velocities below 7 km/s. The effect of this is studied further by calculating state-to-state vibrational relaxation rates, which are shown in Fig. 11. In calculating these rates, it is assumed that translational and rotational energies are in equilibrium at the same temperature,  $T_t = T_r = T$ . Excitation and de-

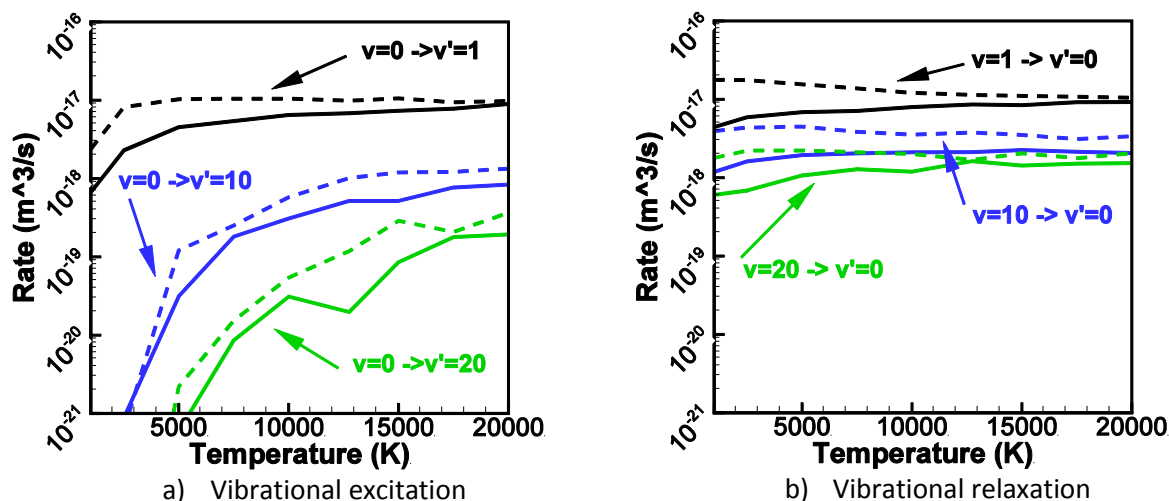


Figure 11: Comparison of state-to-state vibrational rates calculated via the Varandas and Pais (solid lines) and MAP (dashed lines) potentials.

excitation rates produced by the MAP potential are always higher than the rates produced by the ab-initio potential. For instance, the MAP de-excitation rates are a factor of 3 higher at 2,500 K but the differences in rates decreases to 60% at 20,000 K. Likewise, for excitation, the two potentials produce rates that differ by a factor of 3 at 2,500K and by 80% at 20,000 K. Do note that the probability and rates of high  $\Delta v > 10$  transitions are low and therefore they have higher sampling noise. In general, state to state transitions are sensitive to the geometry of the  $O_3$  well and using the simplified MAP PES in the energy range relevant to reentry flight would lead to errors in state-to-state transitions.

## Compact model for dissociation

The  $O_2+O \rightarrow 3O$  dissociation cross sections are shown in Fig. 6. These cross sections depend on relative translational energy, as well as vibrational and rotational energies. A complete set of dissociation cross sections needs to contain  $\sim 2800 \cdot N_{vel}$  elements, where  $N_{vel}$  is the number of velocity intervals. For reactions caused by diatom-diatom collisions, the cross section dataset would increase to  $\sim 2800^2 \cdot N_{vel}$  elements. Sampling large cross section tables within DSMC and CFD would lead to increased computational costs. Instead, these cross sections are fit as:

$$P(E_c, v, J) = A(v, J) (E_c / D)^{\alpha_1(v, J)} (1 - D / E_c)^{\alpha_2(v, J)}, \quad (26)$$

where  $E_c$  is the total collision energy in eV and  $D$  is the dissociation energy. This model requires two fitting parameters:  $A$  and  $\alpha_2$ , and  $\alpha_1$  is maintained at -0.8. These parameters are fit for the Varandas and Pais potential with  $v=[0,10,20,30, 40]$ ,  $J=[11,51,101,151,201,231]$ ,  $V_r=[1, 3, 5, 7, 9, 11, 13, 15, 17]$  km/s levels and linearly interpolated for other levels. The fit of dissociation probabilities are compared to QCT calculations in Fig. 12 This fit match the QCT probabilities within 2%. State-specific rates can be calculated by integrating the dissociation probabilities over the Maxwell velocity distribution. These rates for  $T=10,000$  K and specified ro-vibrational levels are shown in Fig. 13. Although the rates calculated directly via QCT have significant sampling noise, the fit model reproduces the correct trends. The fits for ro-vibrational levels that had to be interpolated also fall within the noise of directly calculated rates.

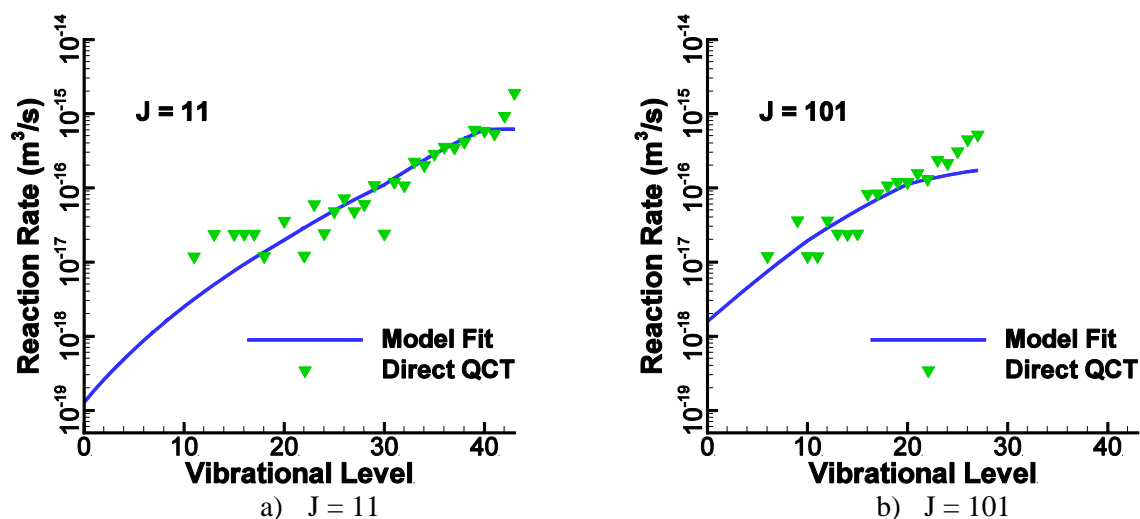


Figure 13: Comparison of modeled and QCT calculated state-specific dissociation rates for  $T = 10,000\text{K}$

The fit of dissociation cross sections can be further verified by calculating the equilibrium dissociation rates. This comparison of dissociation rates calculated via the fit and via direct QCT calculations is shown in Fig. 14. The fitted rates are within 1 standard deviation sampling uncertainty of the directly calculated rates. Therefore, dissociation cross sections can be modeled efficiently using Eq. 24

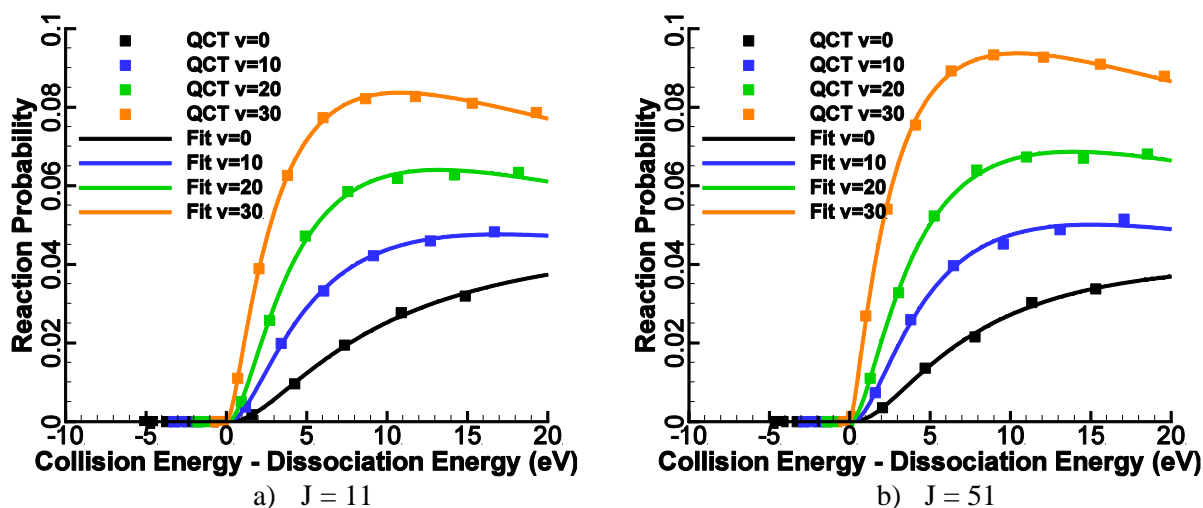


Figure 12: Fit of dissociation probabilities

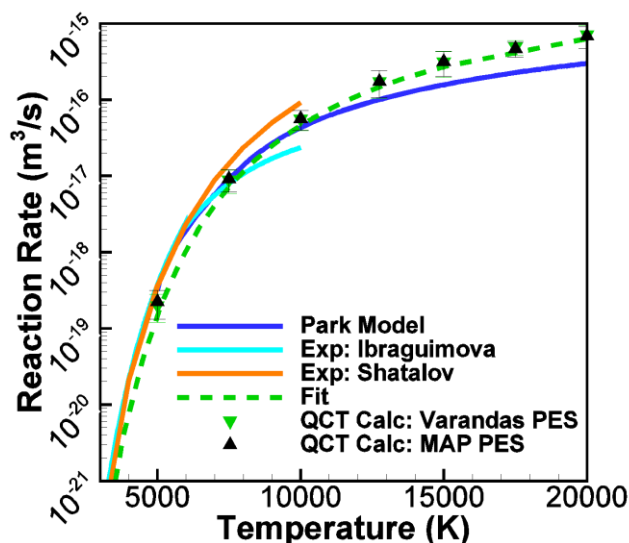


Figure 14: Equilibrium dissociation rate calculated via direct QCT and via the fit model. The error bars represent 1 standard deviation sampling uncertainty

## Compact model for state-to-state energy exchange

DSMC simulations need state-to-state cross sections to describe probabilities of internal energy exchange during collisions. Since oxygen has 2,800 ro-vibrational levels,  $O_2+O$  collisions need to be described by  $2800^2 \cdot N_{vel}$  cross sections. This dataset would grow to roughly  $2800^4 \cdot N_{vel}$  elements for  $O_2+O_2$  collisions. Not only is it computationally infeasible to calculate that dataset with acceptable sampling noise sampling levels but the memory requirements to store such data for all possible collisional partners in the flow and cost of sampling that table during flow calculations are unrealistic. Therefore a reduced state-to-state model is needed to connect ab-initio cross section calculations to flowfield simulations. A new state-to-state model is proposed here based on the maximum entropy (ME) considerations. (Levine and Bernstein 1987). A similar approach has been previously adapted to high enthalpy non-equilibrium flow calculations by Gallis and Harvey (Gallis and J. 1998) and Doraiswamy et al. (Doraiswamy, J. and G. 2013) Those authors; however, did not have access to QCT-calculated cross sections so they introduced a parameter that was adjusted to reproduce macroscopic reaction rate measurements. Our QCT calculations allow us to further develop the ME approach. According to the ME model collisions should lead to distributions that would maximize entropy. This condition is satisfied by equilibrium distribution functions,  $P_0(v)$ . Detailed collision dynamics; however, introduce a constraint on final distribution functions,

$$P(v) = P_0(v) \exp(-S). \quad (27)$$

The surprisal function,  $S$ , describes the how final distributions deviations from the one with maximum entropy. Levine and Gallis used linear surprisal functions. Our calculations, on the other hand, indicate that collisions that have small  $\Delta v$  transitions are more likely to occur. We can also observe that collisions that have high translational energies have reduced interaction time and therefore less energy exchange. Therefore we propose the following surprisal form for state-to-state vibrational energy exchange:

$$S = A |\varepsilon_v - \varepsilon_{v'}| + (B_1 + B_2 \varepsilon_c) \exp \left( - \left| \frac{\varepsilon_v - \varepsilon_{v'}}{C_1 + C_2 \varepsilon_c} \right|^D \right), \quad (28)$$

where  $A$ ,  $B_1$ ,  $B_2$ ,  $C_1$ ,  $C_2$ , and  $D$  are fitting coefficients. This surprisal biases toward small  $\Delta v$  transitions and the amount of biasing depends on the total energy of the collision. The state-to-state cross sections can then be computed as:

$$\begin{aligned} \sigma(v, \varepsilon_i \rightarrow v') &= \sigma_T(\varepsilon_i) P(v, \varepsilon_i \rightarrow v') \\ \sigma_T(\varepsilon_i) &= \sigma_{ref} \varepsilon_i^{\gamma-1} \\ P(v, \varepsilon_i \rightarrow v') &= (1 - \frac{\varepsilon_{v'}}{\varepsilon_c})^\gamma \exp(S) / \sum_{v'} (1 - \frac{\varepsilon_{v'}}{\varepsilon_c})^\gamma \exp(S) \end{aligned} \quad (29)$$

where  $\gamma$  and  $\sigma_{ref}$  are additional fitting parameters. In Eq. 27,  $\varepsilon_c$  and  $\varepsilon_v$  are total collision and post collision vibrational energies. It can be shown that the cross section form in Eq. 27 satisfied micro reversibility and therefore would automatically satisfy detailed balance under equilibrium conditions. A similar approach is used to fit ro-vibrational levels although they are not presented in this report. The eight needed parameters are obtained by minimizing the difference between QCT cross sections and modeled cross sections at  $V = [0, 1, 5, 7, 10, 15, 20, 25, 30]$ ,  $J = [11, 51, 101, 151]$ , and  $V_r = [0.5, 1, 3, 5, 7, 9, 11, 13, 15]$  km/s. The global fit of cross sections is compared to selected QCT cross sections in Fig. 15. The shown cross sections span collision energies of 2 order of magnitude, from 0.06 eV to 6.7 eV. As can be seen, the global fit captures most relevant global trends. Individual modeled cross sections for 0.06 eV translational energies deviate from QCT cross sections by up to 60 %, however as translational energies increase the comparison improves. For 6.7 eV collision energies individual cross sections deviate by less than 30%.

The ME model is used to calculate state-specific vibrational relaxation rates, which are then compared to rates produced by direct QCT calculations with the Varandas and Pais potential. This comparison is shown in Fig. 16a for vibrational relaxation and Fig. 16b for vibrational excitation. In general the vibrational relaxation rates match within 50% above 5,000K and vibrational excitation rates match within 40 % above 5,000K. Throughout this temperature span vibrational rates span 10 orders of magnitude. Below 5,000K vibrational relaxation rates are within 60%. The authors believe the comparison may be improved through further development of the ME model.



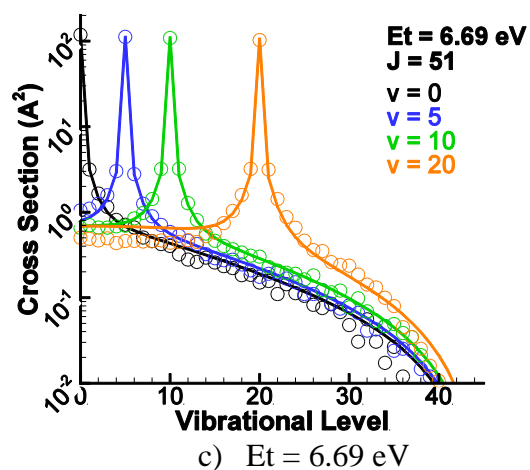
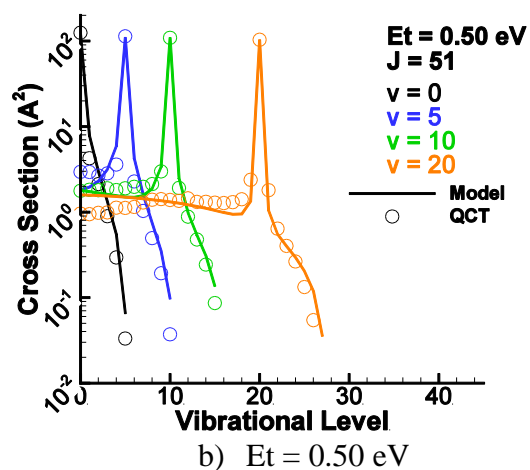
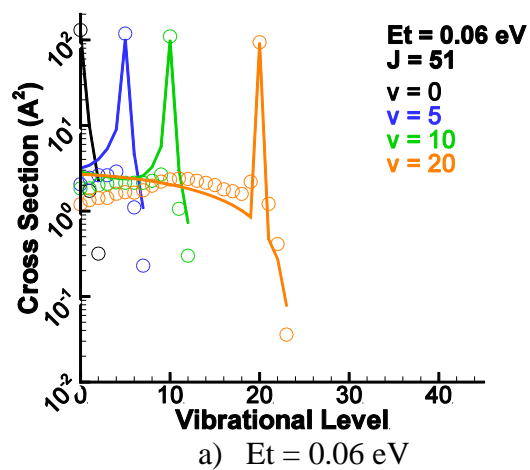


Figure 15: Comparison of modeled and direct QCT-calculated vibrational state-to-state cross sections. The lines are for the modeled cross sections and QCT cross sections are shown as circles.

The model offers a convenient way to upscale ab-initio calculations to DSMC simulations. By using this model, QCT calculations can be run for a set of initial vibrational, rotational and translational energies, which are then fit to the model. The fit of the model is improved by including additional cross section calculations. This model also predicts state-to-state vibrational cross sections using just 8 parameters. In contrast a table of all state-to-state vibrational cross sections would be over  $2000 \times N_{\text{vel}}$  elements.

## ANTICIPATED IMPACT:

Nonequilibrium flows are generated in many engineering applications; however, many models used to calculate such flows are phenomenological. These models are calibrated to reproduce low-temperature equilibrium measurements and then extrapolated to high temperature nonequilibrium conditions. Although ab-initio approaches capable of describing nonequilibrium conditions are available, many difficulties exist in staling these models to full flowfield modeling. The work presented in this report addresses these difficulties in developing state-specific models. The first challenge stems from lack of ab-initio potentials for many needed collision partners. This report shows that since high enthalpy collisions are not highly sensitive to detailed features in potential surfaces, Morse additive pairwise (MAP) potentials may be constructed for collision pairs for which potential surfaces do not exist. Once ab-initio surfaces do become available they can be switched out for MAP surfaces. If resources for calculating ab-initio potentials do exist then it is recommended that more effort is devoted to calculating short-range repulsive part of the potentials, since these have a larger effect on collision outcomes. This approach will allow efficient calculation of state-specific models for complex flows.

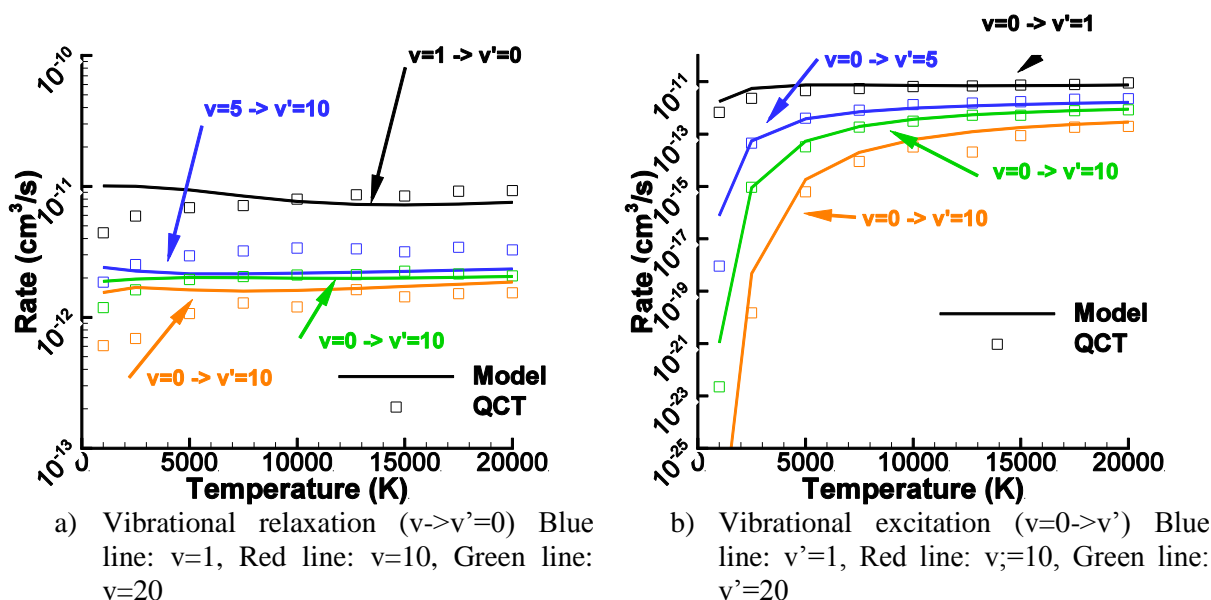


Figure 16: Comparison of state-specific vibrational relaxation rates calculated via the ME model and direct QCT calculations. Translational and rotational temperatures are assumed to be in equilibrium at specified temperature.

The second challenge is caused by high dimensionality of state-to-state cross sections. Since diatomic molecules have 1000s of ro-vibrational levels, the QCT-calculated state-to-state cross sections are on the order of  $1000^2$  for diatom-atom collisions and  $1000^4$  for diatom-diatom collisions. Therefore, an approach was developed in this work to fit dissociation and state-to-state vibrational energy exchange cross sections to a new model based on maximum entropy. The latter model reduced a dataset of  $(46)^2 * N_{\text{vel}}$  vibrational cross sections to just 8 parameters. This model satisfies micro-reversibility and produces necessary detailed balance at equilibrium conditions. Although these models have been used to describe  $\text{O}_2 + \text{O}$  collisions, the models are general enough for any diatomic-monoatomic collisions. The cross section models can be used directly within DSMC calculations and for CFD calculations the cross sections can be integrated to produce vibrational relaxation and dissociation rates. The state-to-state vibrational model is currently being extended to include ro-vibrational levels. Once completed, the parameters for state-to-state and dissociation model will be published for  $\text{O}_2 + \text{O}$ . In addition the model will also be applied to  $\text{N}_2 + \text{N}$  collisions that have been calculated by Jaffe et al. (Jaffe, Schwenke and Chaban 2009)

This report shows a pathway for incorporation ab-initio calculations of atom-diatom collisions within DSMC and CFD simulations. The presented models are as computationally efficient as traditional DSMC models and once incorporated flowfields could be computed with higher fidelity. At Sandia, the work presented can be most directly applied to the Sparta DSMC code developed by Michael Gallis and Steven Plimpton. Total collision energy reaction model and Larsen-Borgnakke relaxation models for  $\text{O}_2 + \text{O}$  can be replaced by the recommended models and dataset for the remaining species could be built up by using MAP potentials recommended in this work.

By comparing QCT-based dissociation calculations to the Park's phenomenological dissociation model, which is used in NASA DPLR and other hypersonic CFD codes, we identified that the Park model is accurate in vibrationally-hot conditions but it may be inaccurate in vibrationally-cold conditions. Since vibrational energies relax slower than translational energies, the vibrationally-

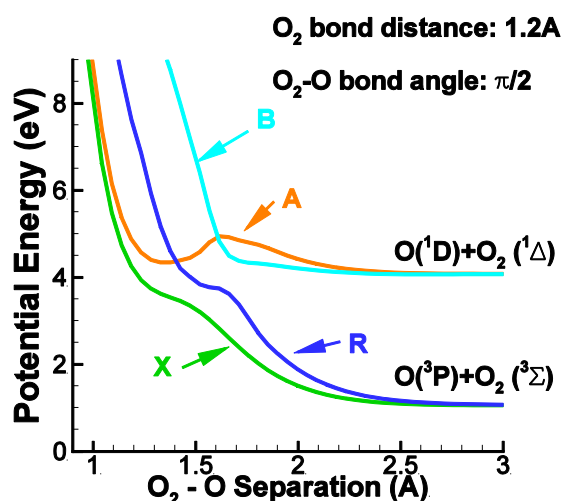


Figure 17: O<sub>3</sub> diabatic potential energy surface for excited states

cold conditions are found in typical compression shocks. Under predicting oxygen dissociation rates within the shocks will lead to higher shock region temperatures and increased convective surface heating. Since atomic oxygen emits strongly in VUV spectrum, under predicting the dissociation rates will also lead to under prediction of VUV radiative heating. Therefore, it is recommended that Park dissociation model in CFD is replaced by ab-initio-based models.

Current work still needs to be extended further. Since free stream conditions are primarily composed on diatoms ( $O_2$  and  $N_2$ ), the presented models need to be adapted for diatom-diatom collisions. This extension can still use the maximum entropy considerations, Eq. 25; however, it may require modification of surprisal function in Eq. 26.

Although current work considered oxygen collisions, the QCT calculations were performed with a single surface. Oxygen; however, has low-lying excited electronic states that can become excited during collisions. Four potential surfaces that correlate to two oxygen states can be seen in Fig. 17. Ignoring electronic excitations of oxygen leads to a significant under prediction of dissociation cross sections and rates, as is shown in Fig. 18. The effect of electronic excitation is considered used the recommendation by Nikitin (see page 11). However, a more rigorous evaluation of electronic excitations is needed. This is currently being investigated by performing surface-hopping trajectory calculations (Sholl and Tully 1998) on 4 excited surfaces that were calculated by McBane et. al. (McBane, Nguyen and Schinke 2010)

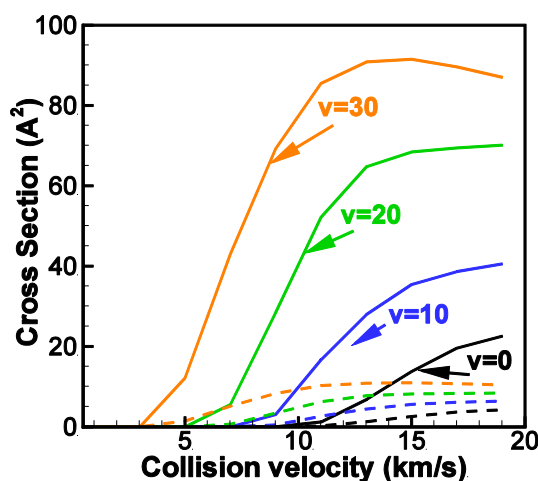


Figure 18:  $O_2+O \rightarrow 3O$  state-specific dissociation cross section with (solid) and without (dashed) electronic corrections

## CONCLUSION:

Our work focused on adapting ab-initio calculations of potential energy surface to direct simulation Monte Carlo (DSMC) and CFD simulations of flowfields. A quasi-classical trajectory (QCT) code is developed and is used to calculate  $O_2+O$  collision at temperatures up to 20,000K. These calculations produced state-specific dissociation cross sections and state-to-state ro-vibrational energy exchange cross sections that are used within DSMC. The cross sections can be integrated to produce rates that are needed for CFD calculations. Two challenges are identified in linking ab-

initio calculations to flowfield simulations for any general chemical systems. First, ab-initio surfaces are not available for all combination of species found in nonequilibrium flows and the quality of available surfaces are not well known. Therefore the sensitivity of rates and cross sections is studied in this work by compare calculations with ab-initio potentials to calculations with Morse additive pairwise (MAP). The MAP potential is constructed from 2-body Morse potentials with parameters that are based on spectroscopic measurements. The equilibrium rates calculated via MAP and ab-initio potentials agree within 12% at temperatures between 2,500 K and 5,000 K. The agreement in dissociation rates improves at temperatures up to 10,000 K. In contrast, the difference between  $O_2+O$  experimental equilibrium rate measurements is 300 % at 10,000 K. Under nonequilibrium conditions, the QCT calculations based on the two potentials match within 70 % while the current phenomenological models disagree by over two orders of magnitude. The simpler MAP potential predicts higher vibrational and rotational de-excitation at low collision velocities but this agreement also improves as collision energies increase. The excitation and de-excitation rates calculated via the two potentials may differ by up to a factor of 3.

In the absence of an ab-initio potential energy surface, a MAP potential may be constructed from spectroscopic measurements to study high enthalpy dissociation and energy exchange processes. The uncertainty in dissociation rates produced by using the simpler potential energy surface is lower than discrepancies in phenomenological models, which are currently used in DSMC and CFD simulations. However, vibrational and rotational state-to-state data is affected by the topology of  $O_3$  potential well. An ab-initio potential is preferred for studying detailed state-to-state collision dynamics.

The second challenge in upscaling ab-initio calculations to flowfield simulations is the high dimensionality of final produced state-specific and state-to-state cross sections. Since oxygen has  $\sim 2,800$  ro-vibrational levels it would need  $\sim 2,800^2 \cdot N_{vel}$  cross sections. This would increase further for diatom-diatom collisions. Therefore this work proposed a new model to fit state-specific dissociation rates and a model to fit state-to-state cross sections based on the maximum entropy considerations. The fitted dissociation cross sections are accurate within 2% and they reproduce equilibrium dissociation rates within sampling uncertainty. The modeled state-to-state cross sections reproduce state-to-state relaxation rates within 50% at temperatures below 5,000K and within 30% at temperatures above 5,000K.

## REFERENCES:

- Bertin, John. 1994. *Hypersonic aerothermodynamics*. AIAA.
- Bird, Graeme. 1994. *Molecular gas dynamics and the direct simulation of gas flows*. Clarendon.
- Bird, Graeme. 2011. "The QK model for gas-phase chemical reaction rates." *Phys. Fluids* 23.
- Braunstein, M., S. Adler-Golden, B. Maiti, and G Schatz. 2003. *Quantum and classical studies of the  $O(3P) + H_2(v = 0 - 3, j = 0) \rightarrow OH + H$  reaction using benchmark potential surface*. Technical Report, DTIC Document,.
- Brunsvold, A., P. Upadhyaya, J. Zhang, R. Cooper, T. Minton, M. Braunstein, and J. Duff. 2008. "Dynamics of hyperthermal collisions of  $O(3P)$  with  $CO$ ." *J. Phys. Chem A*. 112 2192-2205.
- Byron, S. 1959. "Measurement of the rate of dissociation of oxygen." *J. Chem. Phys.* 30 1380.

- Doraiswamy, S., Kelley J., and Candler G. 2013. "Generalized Chemistry-Internal Energy Coupling Model Using Prior Recombination Distribution." *J. Thermophysics and Heat Transfer* 27 382-390.
- Esposito, F., and M. Capitelli. 2002. "Quasiclassical trajectory calculations of vibrationally specific dissociation cross-sections and rate constants for the reaction  $O + O_2(v) \rightarrow 3O$  ." *Chem. Phys. Lett.* 364 180-187.
- Esposito, F., and M. Capitelli. 2006. "QCT calculations for the process  $N_2(v) + N \rightarrow N_2(v') + N$  in the whole vibrational range." *Chem. Phys. Lett.* 418 581-585.
- Esposito, F., I. Armenise, G. Capitta, and M. Capitelli. 2008. "O – O<sub>2</sub> state-to-state vibrational relaxation and dissociation rates based on quasiclassical calculations." *Chem. Phys.* 351 91-98.
- Gallis, M., and Harvey J. 1998. "The modeling of chemical reactions and thermochemical nonequilibrium in particle simulation and computations." *Phys. Fluids* 10.
- Gallis, M., Bond R., and J. Torczynski. 2010. "Assessment of collisional-energy-based models for atmospheric species reactions in hypersonic flows." *J. Thermophys. Heat Transfer* 24 241-253.
- Gilbert, M., A. Gonzalez, F. Mota, and R. Sayos. 1992. "Dynamics of the  $N(4S_u) + NO(X^2\Pi) \rightarrow N_2(X^1\Sigma) + O(3P_g)$  atmospheric reaction on the 3A ground potential energy surface. I. Analytical potential energy surface and preliminary quasiclassical trajectory calculations." *J. Chem. Phys* 97 5542–5553.
- Gimelshein, N., D. Levin, and S. Gimelshein. 2003. "Hydroxyl formation mechanisms and models in high-altitude hypersonic flows." *AIAA* 41 1323-1331.
- Haas, B, and I Boyd. 1993. "Models for direct Monte Carlo simulation of coupled vibration–dissociation." *Phys. Fluids A* 5 478–489.
- Harris, Hamilton, Daniel Millman, and Robert Greendyke. 1992. "Finite-difference solution for laminar or turbulent boundary layer flow over axisymmetric bodies with ideal gas, CF<sub>4</sub>, or equilibrium air chemistry." NASA STI/Recon Technical Report N 93.
- Hirst, M. 1985. *Potential Energy Surfaces: molecular structure and reaction dynamics*. Taylor Francis.
- Ibragimova, L., A. Sergievskaya, V. Levashov, O. Shatalov, Tunik Y., and I. Zabelinskii. 2013. "Investigation of oxygen dissociation and vibrational relaxation at temperatures 4000–10 800 K." *J. Chem. Phys* 139 034317.
- Jaffe, R., D. Schwenke, and G. Chaban. 2009. "Theoretical analysis of N<sub>2</sub> collisional dissociation and rotation-vibration energy transfer." *47th AIAA Aerospace Sciences Meeting including The New Horizons Forum and Aerospace Exposition*.
- . 2010. "Vibrational and rotational excitation and dissociation in n<sub>2</sub>-n<sub>2</sub> collisions from accurate theoretical calculations." *10th AIAA/ASME Joint Thermophysics and Heat Transfer Conference*.
- Karplus, M., R. Porter, and R. Sharma. 1965. "Exchange reactions with activation energy. I. Simple barrier potential for (H, H<sub>2</sub>)." *J. Chem. Phys* 43 3259-3287.
- Kim, J., and I. Boyd. 2014. "Monte Carlo simulation of nitrogen dissociation based on state-resolved cross sections." *Phys. Fluids* 26.
- Konowalow, D., and J. Hirschfelder. 1961. "Morse potential parameters for O – O, N – N, and N – O interactions." *Phys. Fluids* 4 37.
- Kormann, K., S. Holmgren, and H. Karlsson. 2008. "Accurate time propagation for the schrodinger equation with an explicitly time-dependent hamiltonian." *J. Chem. Physics* 128 184101.
- Koura, K. 1998. "Monte Carlo direct simulation of rotational relaxation of nitrogen through high total temperature shock waves using classical trajectory calculations." *Phys. Fluids* 10 2689-2691.
- Kulakhmetov, M., and A. Alexeenko. 2015. "Sensitivity of state-specific dissociation cross sections to O<sub>3</sub> potential energy surfaces." *53rd AIAA Aerospace Sciences Meeting*.



- Kulakhmetov, Marat. 2014. "Upscaling ab-initio chemistry models to non-equilibrium flow simulations." Ph.D. Preliminary Document, Aeronautics and Astronautics, Purdue University.
- Kulakhmetov, Marat, Alexeenko Alina, Weaver Andrew, Mihaly Slipchenko, Jonathan Mihaly, Mac Adams, and Ares Rosakis. 2012. "Feasibility of Non-Equilibrium Hypersonic Flow Measurements at the Small Particle Hypervelocity Impact Range." *50th AIAA Aerospace Sciences Meeting including the New Horizons Forum and Aerospace Exposition*.
- Lagana, A., E. Garcia, and L. Ciccarelli. 1987. "Deactivation of vibrationally excited nitrogen molecules by collision with nitrogen atoms." *J. Physical Chemistry* 91 312-314.
- Laurendeau, Normand. 2005. *Statistical thermodynamics: fundamentals and applications*. Cambridge University Press.
- Levin, R., and R. Bernstein. 1987. *Molecular Reaction Dynamics and Chemical Reactivity*. Oxford University Press.
- Levine, Ira. 2000. *Quantum chemistry*. Prentice Hall.
- Levine, R., and R. Bernstein. 1987. *Molecular Reaction Dynamics and Chemical Reactivity*. Oxford University Press.
- Maruta, Kaoru. 2011. "Micro and mesoscale combustion." *Proceedings of the Combustion Institute*. 125-150.
- Mathews, D. 1959. "Interferometric measurement in the shock tube of the dissociation rate of oxygen." *Phys. Fluids* 2 170.
- McBane, G., L. Nguyen, and R. Schinke. 2010. "Photodissociation of ozone in the hartley band: Product state and angular distributions." *J. Chem. Phys* 133.
- Nikitin, E. 1974. *Theory of Elementary Atomic and Molecular Processes in Gases*. Clarendon Press.
- Norman, P., P. Valentini, and T. Schwartzentruber. 2013. "GPU-accelerated classical trajectory calculation direct simulation Monte Carlo applied to shock waves." *J. Comput. Phys.* 247 153-167.
- Panesi, M., R. Jaffe, and D. Schwenke. 2013. "Energy transfer study of  $N_2 - N_2$  and  $N_2 - N$  interactions by using rovibrational state-to-state model." *44th AIAA Thermophysics Conference*.
- Park, Chul. 1989. *Nonequilibrium hypersonic aerothermodynamics*.
- Parsons, N., T. Zhu, D. Levin, and A. van Duin. 2014. "Development of DSMC chemistry models for nitrogen collisions using accurate theoretical calculations." *52nd Aerospace Sciences Meeting*.
- Reising, Heath, KC Utsav, Stephen Voelkel, Noel Clemens, Venkatramanan Raman, Philip Varghese, and Heeseok Koo. 2014. "Vibrational Non-equilibrium Effects in Supersonic Jet Mixing." *52nd Aerospace Sciences Meeting*.
- Rink, J., H. Knight, and R. Duff. 1961. "Shock tube determination of dissociation rates of oxygen." *J. Chem. Phys.* 34 1942.
- Sanz-Sarna, J., and A. Portillo. 1996. "Classical numerical integrators for wave-packet dynamics." *J. Chemical Physics* 104 2349-2355.
- Schexnayder, C., and J. Evans. 1961. *Measurements of the dissociation rate of molecular oxygen*. National Aeronautics and Space Administration. Langley Research Center.
- Schinke, R., S. Grebenshchikov, M. Ivanov, and P. Fleurat-Lessard. 2006. "Dynamical studies of the ozone isotope effect: A status report." *Annu. Rev. Phys. Chem.* 57 625-661.
- Sholl, D., and J. Tully. 1998. "A generalized surface hopping method." *J. Chem. Phys* 109 7702-7710.
- Tashiro, M., and R. Schinke. 2003. "The effect of spin-orbit coupling in complex forming  $O(3P) + O_2$  collisions." *J. Chem. Phys* 119 10186-10193.
- Truhlar, D. 1972. "Multiple potential energy surfaces for reactions of species in degenerate electronic states." *J. Chem. Phys* 56 3189-3190.

- Truhlar, D., J. Muckerman, and R. Bernstein. 1979. *Atom-Molecule Collision Theory: A Guide for the Experimentalist* (. Plenum.
- Vanderslice, J., E. Mason, and W. Maisch . 1960. "Interactions between ground state oxygen atoms and molecules: O–O and O2–O2." *J. Chem. Phys* 32 515-524.
- Varandas, A., and A. Pais. 1988. "A realistic double many-body expansion (DMBE) potential energy surface for ground-state O3 from a multiproperty fit to ab-initio calculations, and to experimental spectroscopic, inelastic scattering, and kinetic isotope thermal rate data." *Mo. Phys.* 65 843-860.
- Wadworth, D., and I. Wysong. 1997. "Vibrational favoring effect in DSMC dissociation models." *Phys. Fluids* 9 3873–3884.
- Walch, S., and R. Jaffe. 1987. "Calculated potential surfaces for the reactions: O+ N2, NO+ N and N+ O2 NO+ O." *J. Chemical Physics* 86 6946-6956.
- Wolfgang, Demtroder. 2006. *Atoms, molecules and photons*. Heidelberg.

**Acknowledgement:** The research was supported in part by the Laboratory Directed Research and Development (LDRD) Program at Sandia National Laboratories. Sandia National Laboratories is a multi-program laboratory managed and operated by Sandia Corporation, a wholly owned subsidiary of Lockheed Martin Corporation, for the U.S. Department of Energy's National Nuclear Security Administration under Contract DE-AC04-94AL85000.